PNAS
www.pnas.org

Supplementary Information for

Interfacial Engineering of Cobalt Sulfide/Graphene Hybrids for Highly Efficient Ammonia Electrosynthesis

Pengzuo Chen[§1], Nan Zhang[§2], Sibo Wang[1], Tianpei Zhou[1], Yun Tong[1], Chengcheng Ao[2], Wensheng Yan[2], Lidong Zhang[2], Wangsheng Chu[2], Changzheng Wu*[1], and Yi Xie[1]

Changzheng Wu
Email: czwu@ustc.edu.cn

This PDF file includes:

Methods
Figs. S1 to S28
Tables S1 to S2
References for SI reference citations

Methods

The synthesis of graphene oxide (GO). All of the chemicals were of analytical grade and used without further purification. GO was synthesized from graphite powder by using the modified Hummers' method[S1]. Typically, 1.5 g of graphite powder was added to a 9:1 mixture of concentrated H_2SO_4/H_3PO_4 (180:20 mL), and then 9.0 g $KMnO_4$ was slowly added to the above solution under continuous stirring. Then, the mixed system was heated to 60 °C and maintained for 12 h under continuous stirring. The solution was poured into 200 ml of ice water with 10 ml of H_2O_2 (30%) after cooling to room temperature. The remaining solid product was collected by centrifugation and washed in succession with 200 mL of water, 200 mL of 30% HCl, and 200 mL of ethanol (twice). The as-prepared GO was added to deionized water and continuously ultrasonicated to form a homogenous aqueous dispersion (2 mg ml^{-1}).

The synthesis of MS_2/NS-G, MS/NS-G and NS-G hybrid catalysts. In a typical process, 0.2 mmol metal chloride salt ($CoCl_2 \cdot 6H_2O$, $NiCl_2 \cdot 6H_2O$, $FeCl_3$ or $SnCl_4 \cdot 5H_2O$) was added to 10 ml of deionized water under continuous stirring until complete dissolution. Then, 50 ml of GO (2 mg ml^{-1}) aqueous dispersion was added to the above solution and stirred for 12 h. The MCl_x/GO precursor was obtained through a freeze-drying process from the above solution. Next, 25 mg of the resulting MCl_x/GO precursor was placed at the centre of a tube furnace, and 2.0 g of thiourea was placed at the upstream side near the precursor. Then, the furnace was heated to 500 °C at a

ramping rate of 10 °C min^{-1} under a flowing Ar atmosphere and maintained for 2 h. Finally, the MS_2/NS-G (M=Co, Ni, Fe and Sn) hybrid material was collected after the system was cooled to room temperature. Moreover, the synthetic procedure for MS/NS-G is similar to that for MS_2/NS-G except for the use of 200 mg of thiourea during the annealing treatment. NS-G was prepared by using the same strategy as MS_2/NS-G without adding the metal salt.

Structural Characterization. X-ray powder diffraction (XRD) was performed using a Philips X'Pert Pro Super diffractometer with Cu-Kα radiation (λ=1.54178 Å). Transmission electron microscopy (TEM) was performed on a JEM-2100F field-emission electron microscope operated at an acceleration voltage of 200 kV. Scanning electron microscopy (SEM) images were recorded on a JEOL JSM-6700F SEM. High-resolution TEM (HRTEM), high-angle annular dark-field scanning transmission electron microscopy (HAADF-STEM), and corresponding energy-dispersive X-ray spectroscopy (EDS) mapping analyses were executed on a JEOL JEM-ARF200F TEM/STEM with a spherical aberration corrector. X-ray photoelectron spectra (XPS) were obtained on an ESCALAB MK II X-ray photoelectron spectrometer with Mg Kα as the excitation source. The binding energies obtained in the XPS spectral analysis were corrected for specimen charging by referencing C 1s to 284.5 eV. The absorbance data of the spectrophotometer were measured on an ultraviolet-visible (UV-Vis) spectrophotometer (SOLID3700). Co L-edge, S L-edge, C K-edge and N K-edge XANES spectra were measured at the U19 beam line of the National Synchrotron

Radiation Laboratory (NSRL, Hefei) in total electron yield (TEY) mode by collecting the sample drain current under a vacuum greater than 10^{-7} Pa.

Electrochemical Measurements. The electrochemical tests were carried out in a three-electrode system on an electrochemical workstation (CHI660B) at room temperature. Electrochemical reduction of N_2 to ammonia was performed in a two-compartment cell at room temperature, and the cells were separated by a Nafion 117 membrane. A Ag/AgCl (saturated KCl solution) electrode was used as the reference electrode, and a graphite rod was used as the counter electrode. The cathode was prepared as follows: 4 mg of catalyst powder, 1 ml of alcohol and 40 μl Nafion solution (Sigma Aldrich, 5 wt %) were mixed and sonicated for at least 1 h to form a homogeneous ink. Then, a certain volume of catalyst ink was drop-casted onto carbon paper with a loading of 0.2 mg cm^{-2}. The area of carbon paper electrode is 1 × 2 cm^2 and the practically immersing area in the electrolyte was 1 × 1 cm^2. The electrolyte volume in the two parts of H-cell is 30 ml. For electrocatalytic N_2 reduction, potentiostatic tests were conducted in N_2-saturated 0.05 M H_2SO_4 for 2 h, which was purged with N_2 for 30 min before the measurement. Pure N_2 was continuously fed into the cathodic compartment with a properly positioned sparger during the experiments.

The yield rate of NH_3 formation was calculated as Equation S1, where *c* was the total mass concentration of NH_3, *V* was the volume of the electrolyte, *t* was the reduction reaction time, and *m* was the loading mass of catalysts.

$$r_{NH3} = (c_{NH3} \times V) / t \times m_{cat}. \qquad (S1)$$

The Faradaic efficiency (FE) of NRR was calculated as Equation S2, where *F* was the Faraday constant, *Q* was the charge, and *n* was the total molar weight of NH_3 product.

$$FE = 3F \times n_{NH3} / Q \qquad (S2)$$

Product quantification. The ammonia concentration was spectrophotometrically determined by the indophenol blue method with modification[11,25]. Typically, 2 mL of solution was removed from the cathode electrochemical reaction vessel. Then, 2 mL of a 1 M NaOH solution containing 5 wt% salicylic acid and 5 wt% sodium citrate was added to the electrolyte, followed by the addition of 1 mL of 0.05 M NaClO and 0.2 mL of 1 wt % $C_5FeN_6Na_2O$ (sodium nitroferricyanide) solution. After 2 h at room temperature, the absorption spectrum was measured using a UV-vis spectrophotometer. The formation of indophenol blue was determined using the absorbance at a wavelength of 655 nm. The concentration-absorbance curves were calibrated using standard ammonia chloride solutions containing the same concentrations of H_2SO_4 as those used in the electrolysis experiments (SI Appendix, Fig. S8).

The hydrazine concentration of the electrolyte was estimated by the Watt and Chrisp method[11,12,25]. A mixture of para-(dimethylamino)benzaldehyde (5.99 g), HCl (concentrated, 30 mL) and ethanol (300 mL) was used as a colour reagent. First, 2 mL of solution was removed from the cathode electrochemical reaction vessel. Then, 2 mL of colour reagent was added to the electrolyte, and the absorption spectrum was

measured using a UV-vis spectrophotometer after 30 min at room temperature. The formation of hydrazine was determined using the absorbance at a wavelength of 455 nm. The concentration-absorbance curves were calibrated using standard hydrazine solutions containing the same concentrations of H_2SO_4 as those used in the electrolysis experiments (SI Appendix, Fig. S9).

$^{15}N_2$ isotope labelling experiment. The $^{15}N_2$ gas was purchased from Cambridge Isotope Laboratories, Inc. Before the electrochemical reduction experiment, the electrolyte was purged with high-purity Ar to remove the $^{14}N_2$ from solution and then was pre-saturated with $^{15}N_2$ for 30 min with a flow rate of 5 sccm. After $^{15}N_2$ electrochemical reduction for 20 h at a potential of -0.2 V, the electrolyte was concentrated and the obtained $^{15}NH_4^+$ product was identified using ^1H NMR spectroscopy with water suppression (Bruker AVANCE AV III 400).

S1. Synthesis process of various MS_2/NS-G and MS/NS-G materials

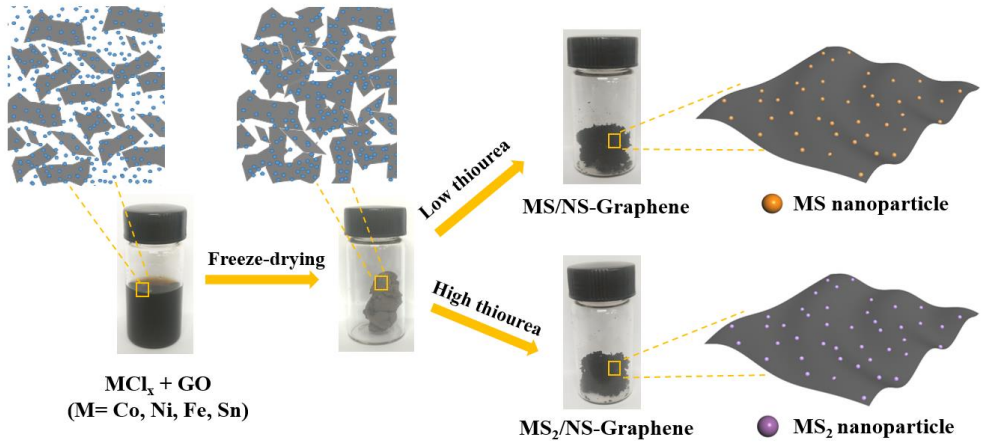

Figure S1 Schematic illustration for the synthesis process of various MS_2/NS-G and MS/NS-G hybrid materials (M= Co, Fe, Ni and Sn).

S2. The XRD pattern and TEM image of NS-G sample

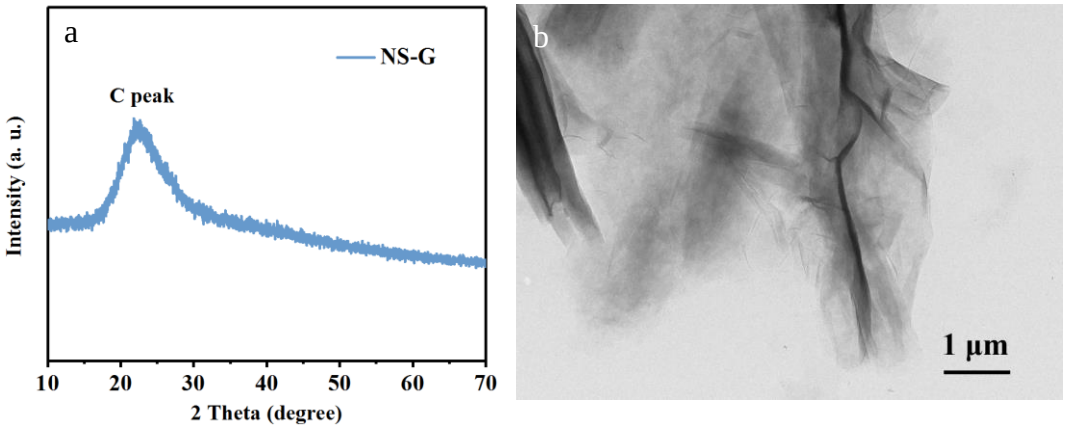

Figure S2 The a) XRD pattern and b) TEM image of as-obtained NS-G product.

S3. XRD patterns of CoS_x/NS-G sample

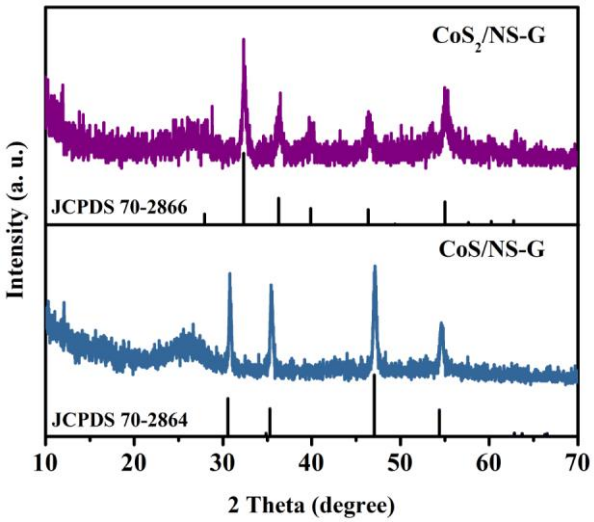

Figure S3 XRD patterns of as-prepared CoS_2/NS-G and CoS/NS-G hybrid materials

S4. TEM characterizations of as-prepared CoS/NS-G sample

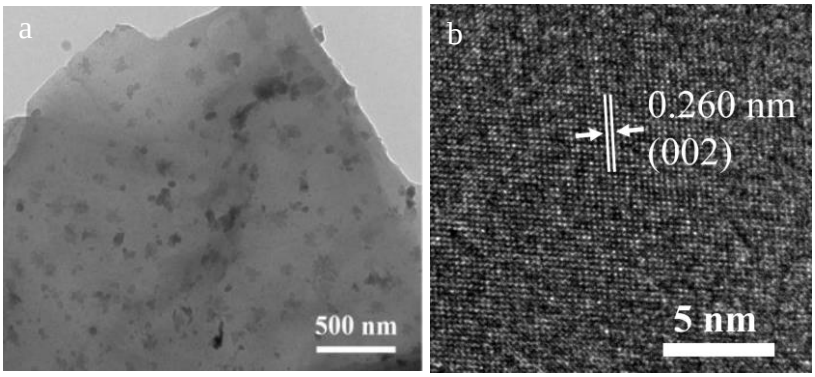

Figure S4 a) TEM image and b) corresponding HRTEM image of CoS/NS-G hybrid product.

S5. The EDS spectrum of as-prepared CoS_2/NS-G product

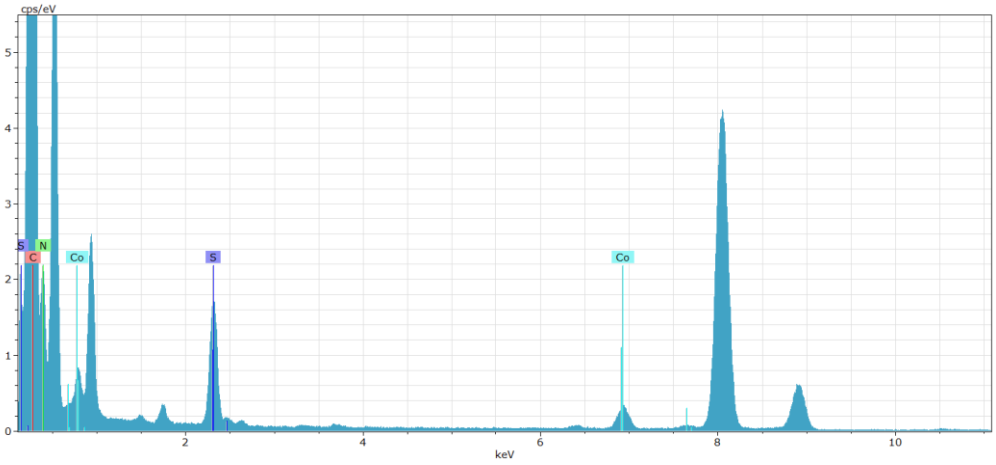

Figure S5 The EDS spectrum of as-prepared CoS_2/NS-G hybrid.

S6. The EDS spectrum and elemental mapping images of CoS/NS-G product

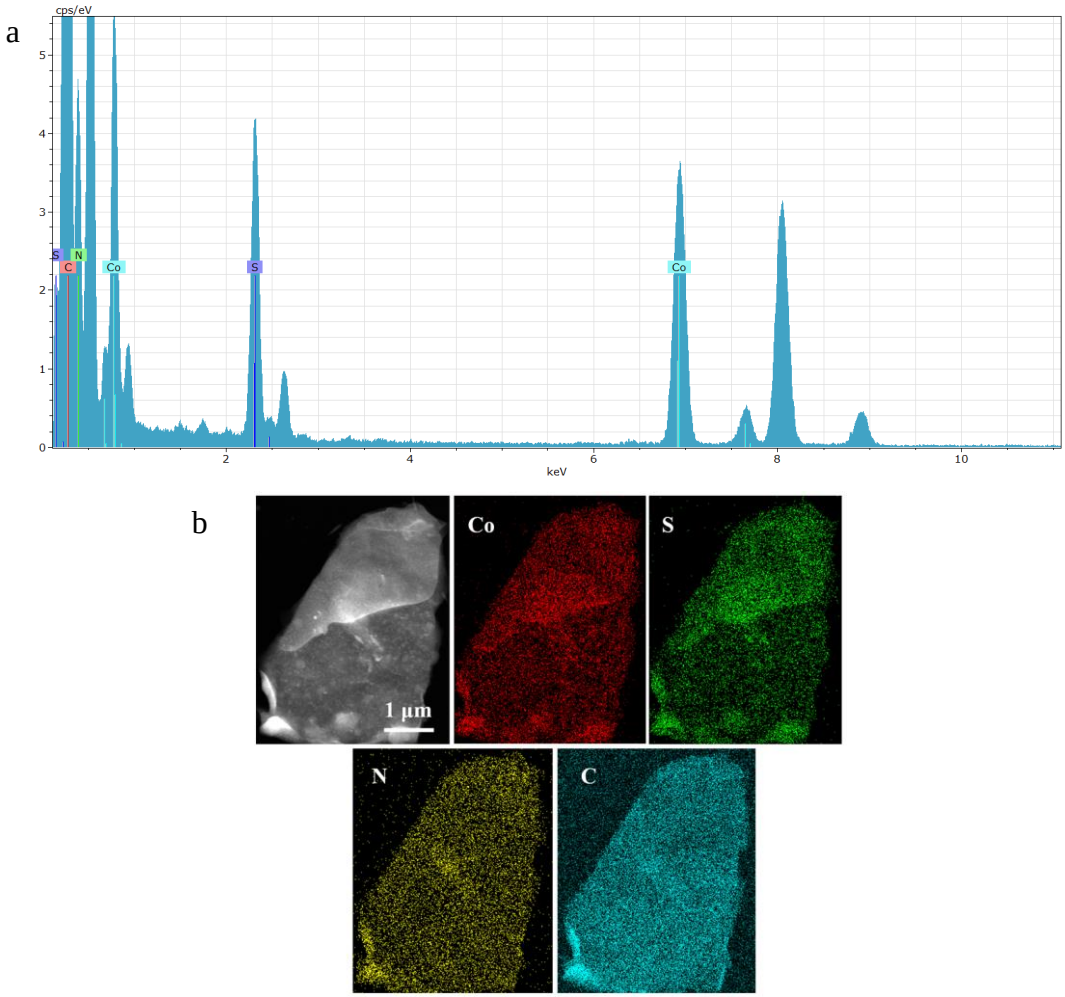

Figure S6 a) The EDS spectrum, b) HAADF-STEM image and corresponding elemental mapping for CoS/NS-G hybrid.

S7. The N 1s spectra of CoS_2/NS-G and CoS/NS-G products

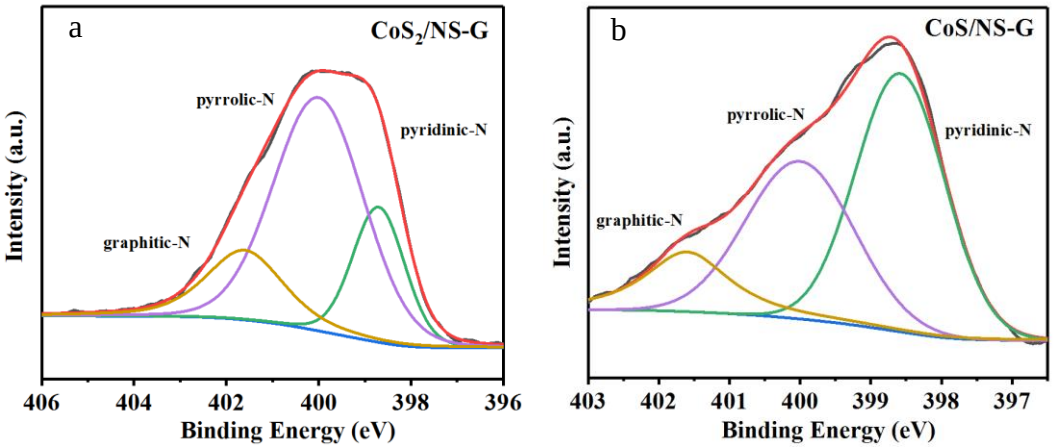

Figure S7 The N 1s spectra for a) CoS_2/NS-G and b) CoS/NS-G hybrids.

S8. Absolute calibration of the indophenol blue method using ammonium chloride solutions of known concentration as standards

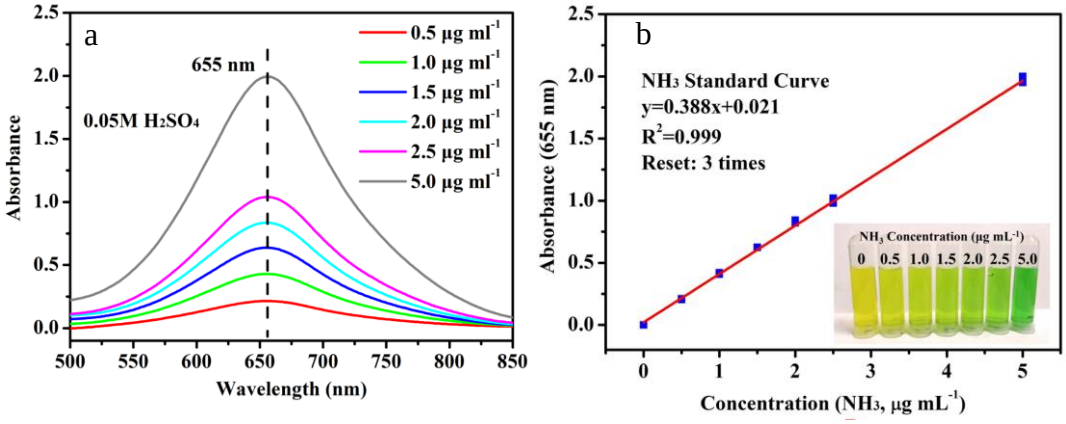

Figure S8 a) UV-vis curves of indophenol assays with NH_4^+ ions after incubated for 2 hours and b) calibration curve used for estimation of NH_3 by NH_4^+ ion of different concentrations. The absorbance at 655 nm was measured by UV-vis spectrophotometer, and the fitting curve shows good linear relation of absorbance with NH_4^+ ion concentration (y = 0.388x + 0.021, R^2=0.999) of three times independent calibration curves. The inset of b) shows the chromogenic reaction of indophenol indicator with NH_4^+ ions.

S9. Absolute calibration of the Watt and Chrisp method using hydrazine hydrate solutions of known concentration as standards

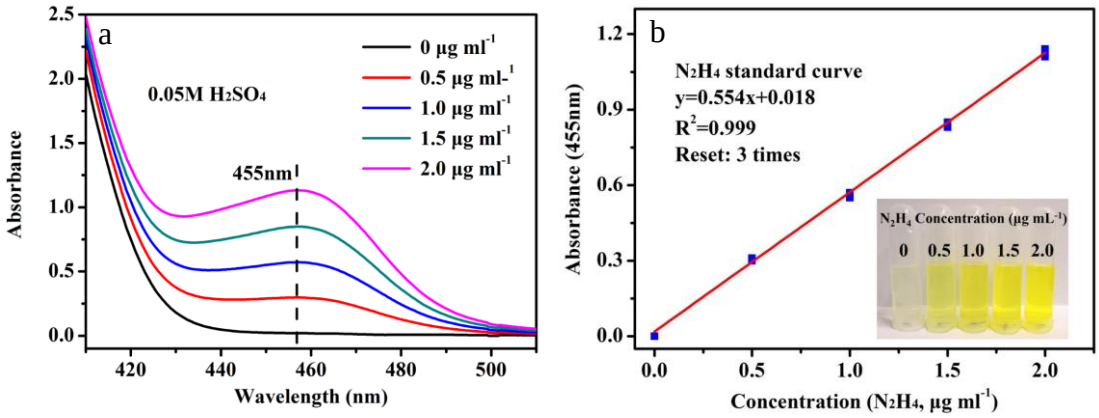

Figure S9 a) UV-vis curves of $N_2H_4 \cdot H_2O$ after incubated for 30 min and b) calibration curve used for estimation of $N_2H_4 \cdot H_2O$ concentration. The absorbance at 455 nm was measured by UV-vis spectrophotometer, and the fitting curve shows good linear relation of absorbance with $N_2H_4 \cdot H_2O$ concentration (y = 0.554x + 0.018, R^2=0.999) of three times independent calibration curves. The inset of b) shows the chromogenic reaction of indicator with $N_2H_4 \cdot H_2O$.

S10. Yield Rate of NH_3 and Faradaic efficiency of CoS/NS-G at each given potential

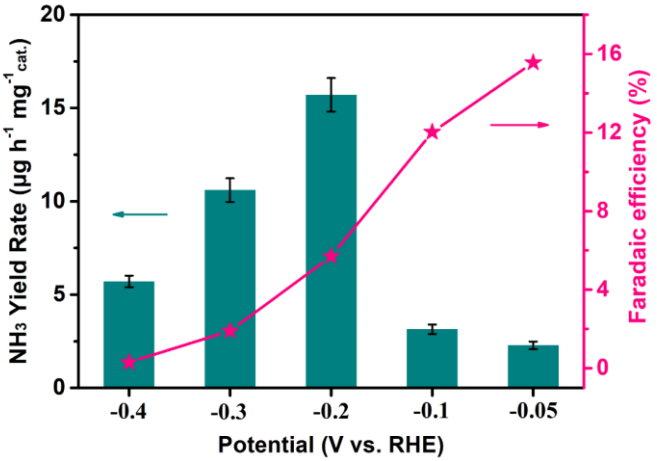

Figure S10 NH_3 yield and Faradaic efficiency of as-prepared CoS/NS-G catalyst at each given potential.

S11. Yield rate of NH_3 for different catalysts at −0.2 V

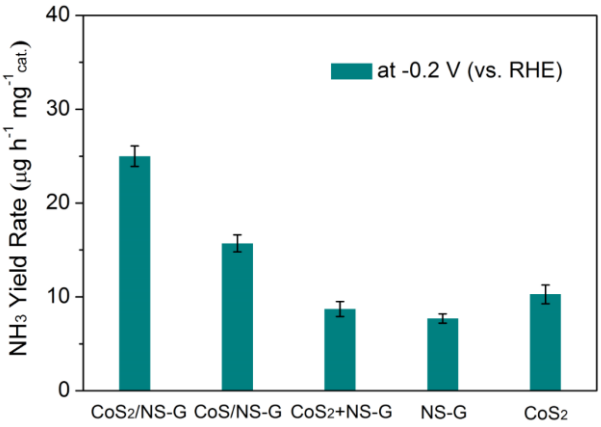

Figure S11 Yield rate of NH_3 for different catalysts at −0.2V (vs. RHE) at room temperature and ambient pressure.

S12. XRD patterns and TEM images of other MS_2/NS-G and MS/NS-G samples

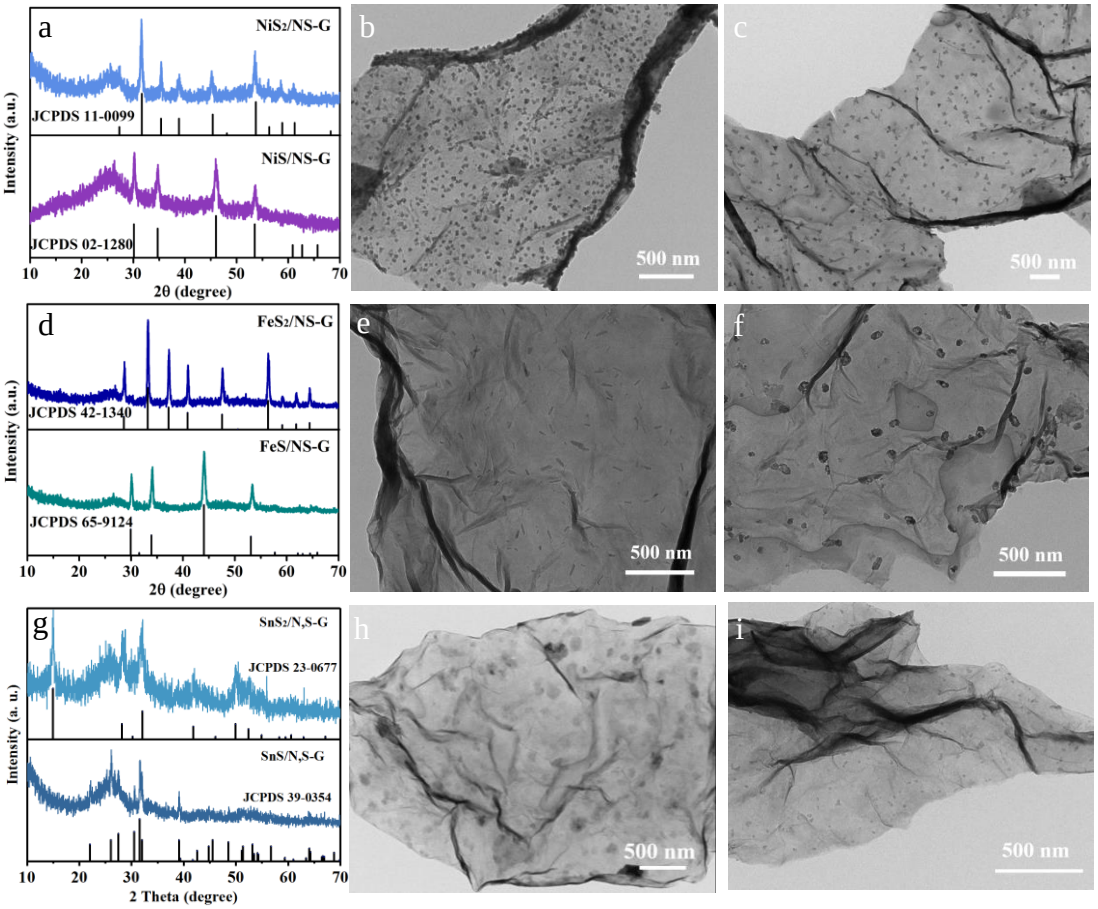

Figure S12 a-c) XRD patterns and TEM images of NiS_2/NS-G and NiS/NS-G hybrids; d-f) XRD patterns and TEM images of FeS_2/NS-G and FeS/NS-G hybrids; g-i) XRD patterns and TEM images of SnS_2/NS-G and SnS/NS-G hybrids.

S13. The XPS spectra of as-prepared NiS_2/NS-G and NiS/NS-G products

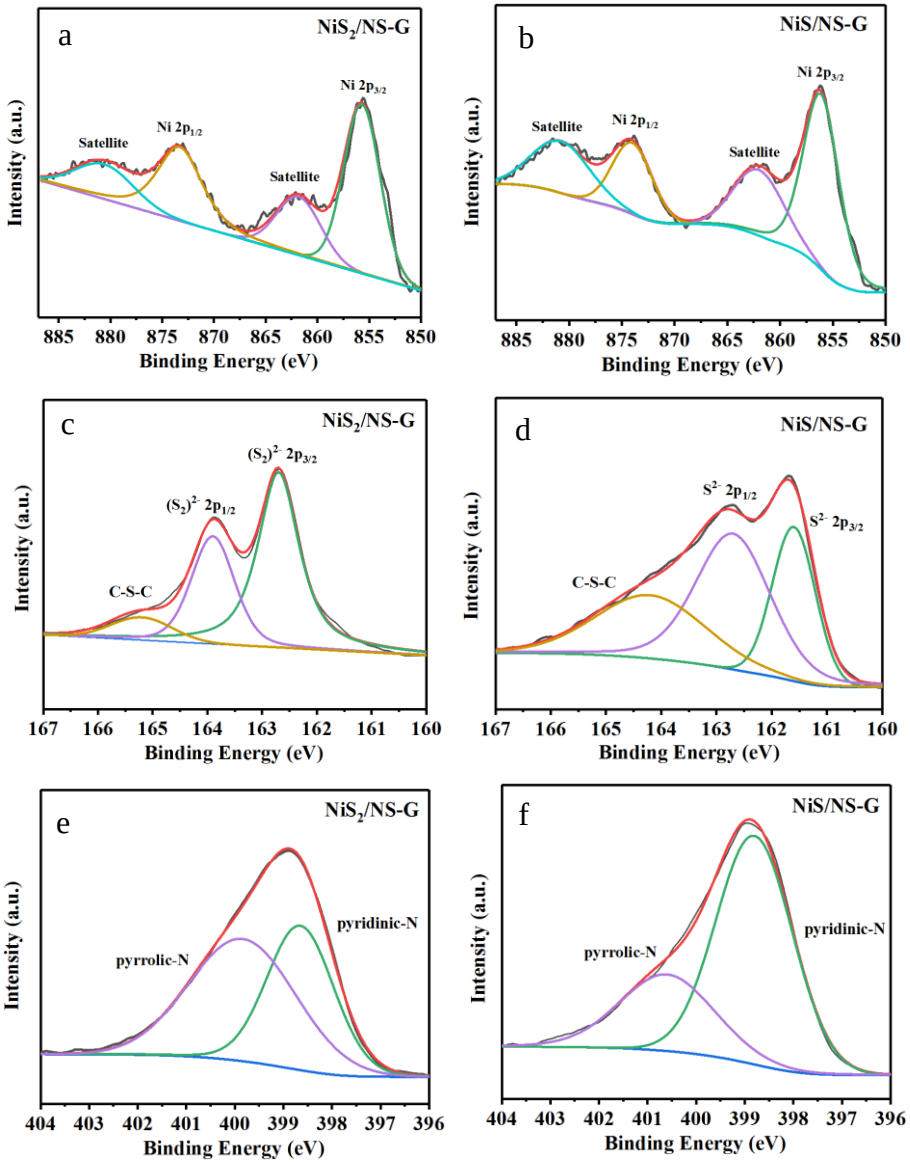

Figure S13 The a-b) Ni 2p, c-d) S 2p as well as e-f) N 1s spectra of as-obtained NiS_2/NS-G and NiS/NS-G hybrid.

S14. The XPS spectra of as-prepared FeS_2/NS-G and FeS/NS-G products

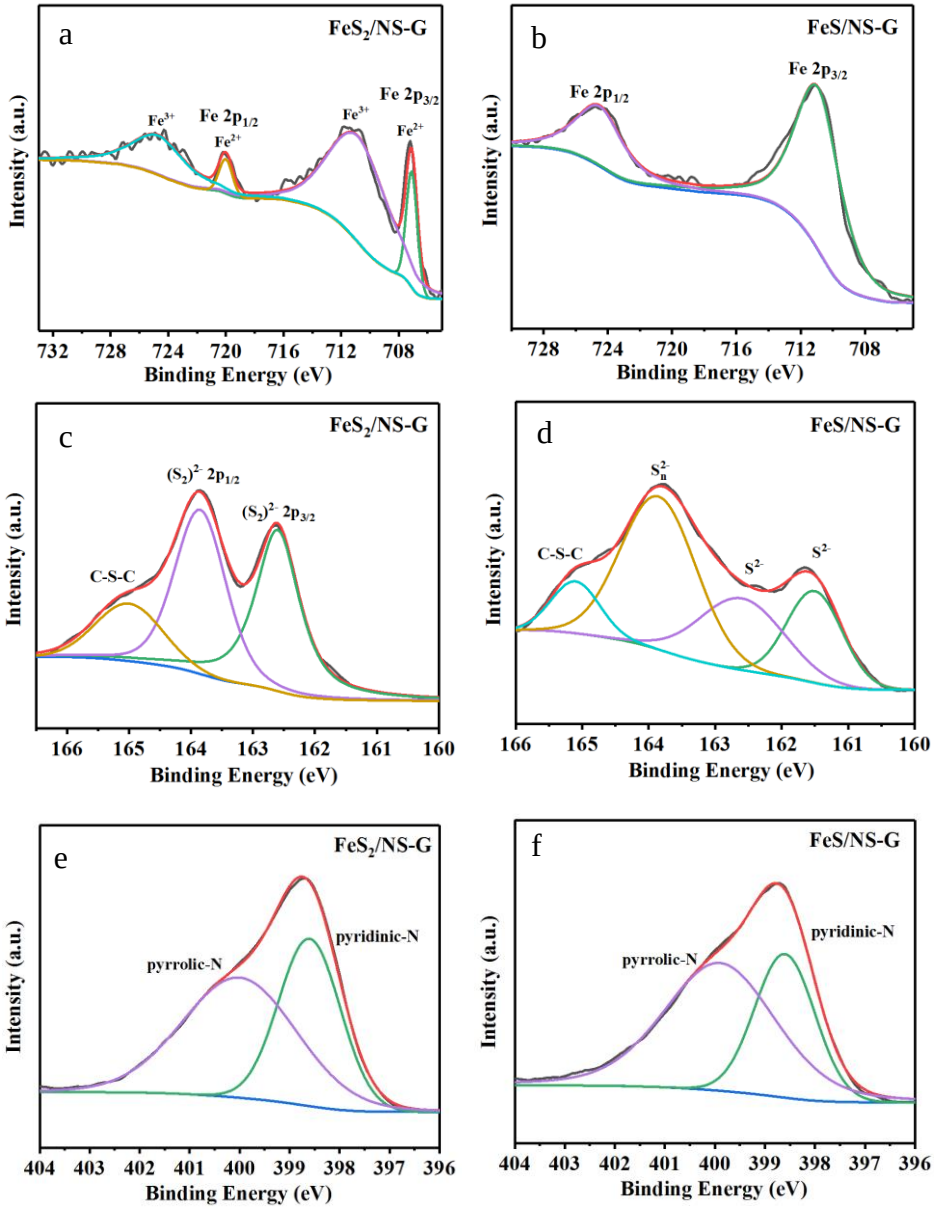

Figure S14 The a-b) Fe 2p, c-d) S 2p as well as e-f) N 1s spectra of as-obtained FeS_2/NS-G and FeS/NS-G hybrid.

S15. The XPS spectra of as-prepared SnS_2/NS-G and SnS/NS-G products

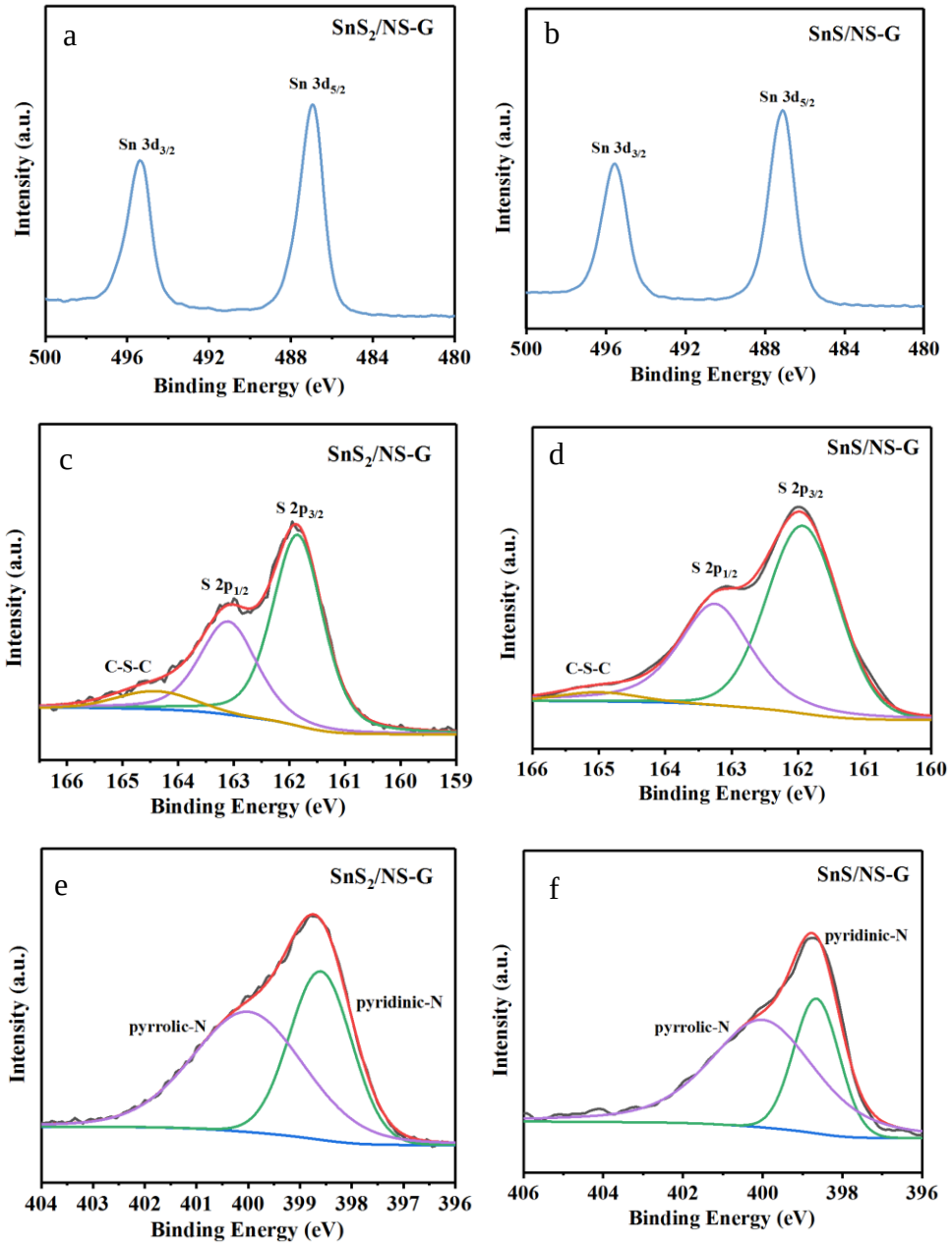

Figure S15 The a-b) Sn 3d, c-d) S 2p as well as e-f) N 1s spectra of as-obtained SnS_2/NS-G and SnS/NS-G hybrid.

S16. Comparison of NH_3 yield rate for other strong coupled hybrids.

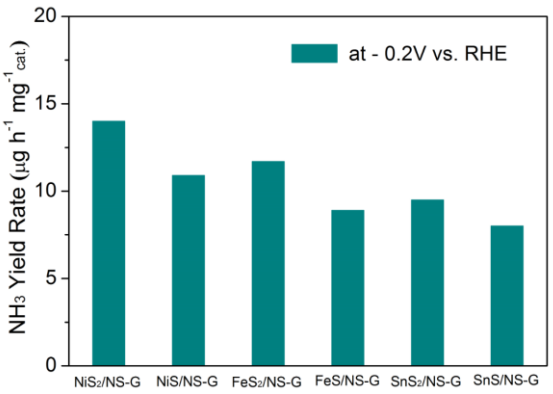

Figure S16 Comparison of NH_3 yield rate for other strong coupled hybrids.

S17. TEM images and particle size distribution of CoS_2/NS-G hybrids synthesized by different amount of cobalt salt.

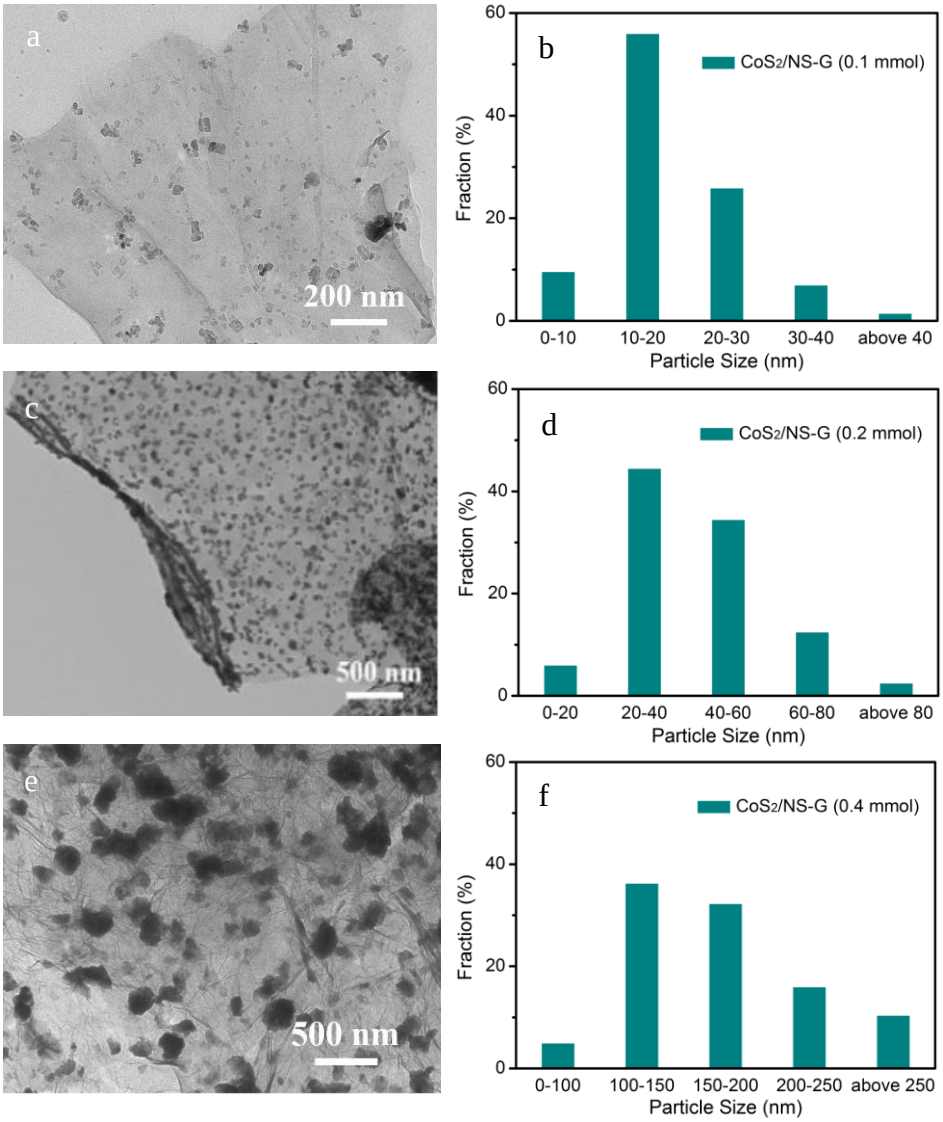

Figure S17 TEM images and particle size distribution of CoS_2/NS-G hybrids synthesized by different amount of cobalt salt: a-b) 0.1 mmol $CoCl_2$; c-d) 0.2 mmol $CoCl_2$; e-f) 0.4 mmol $CoCl_2$.

S18. Chronoamperometric response of as-prepared CoS_2/NS-G hybrid.

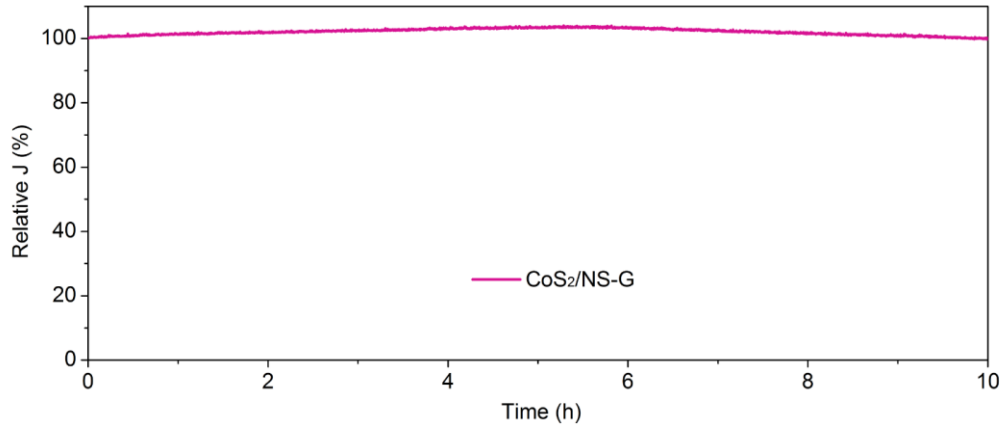

Figure S18 Chronoamperometric response of as-prepared CoS_2/NS-G catalyst in N_2-saturated 0.05M H_2SO_4 solution.

S19. TEM image of CoS_2/NS-G catalyst after NRR test.

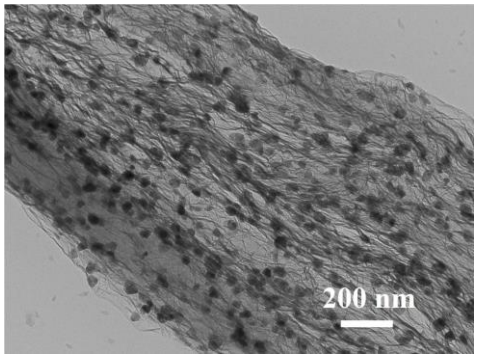

Figure S19 TEM image of CoS_2/NS-G hybrid after NRR test.

S20. The XPS spectra and XRD patterns of as-prepared CoS_2/NS-G before and after NRR test.

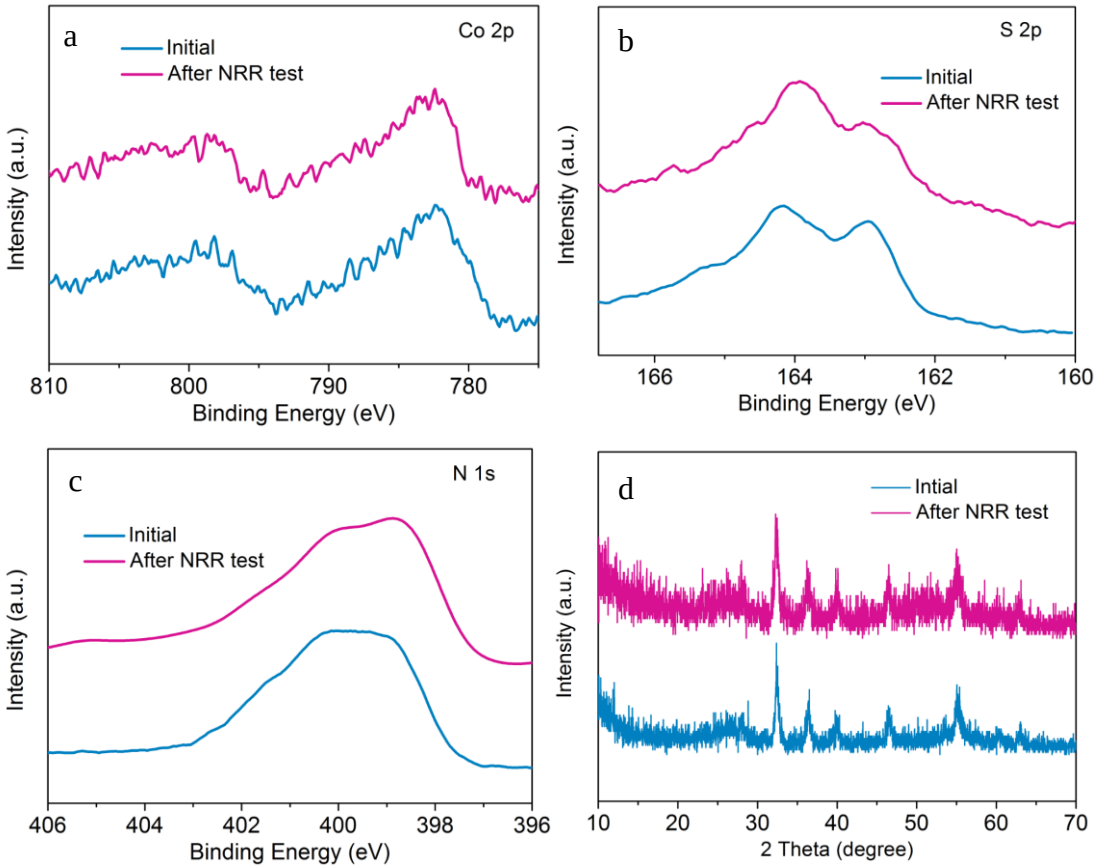

Figure S20 High-resolution XPS spectra of a) Co 2p, b) S 2p and c) N 1s and d) XRD patterns for the CoS_2/NS-G hybrid before and after NRR test.

S21. Schematic illustration for NH_3 electrosynthesis by catalysts of CoS_x/NS-G under ambient conditions.

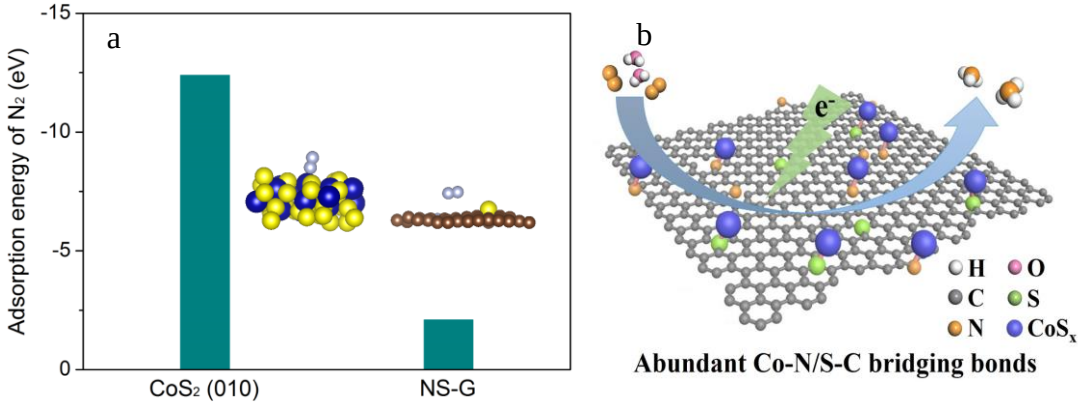

Figure S21 a) Optimized structures of the systems formed by adsorbing a nitrogen and comparison of nitrogen adsorption energy for CoS_2 and NS-G (Co: blue; S: yellow; C: brown; N: gray). b) Schematic illustration for NH_3 electrosynthesis by catalysts of CoS_x/NS-G under ambient conditions.

First-principle calculations were performed by the density functional theory (DFT) using the Vienna Ab-initio Simulation Package (VASP) package[S2]. The generalized gradient approximation (GGA) with the Perdew-Burke-Ernzerhof (PBE) functional was used to describe the electronic exchange and correlation effects[S3]. The K points meshing for Brillioun zone was set up as a 3 × 3 × 1 grid Monkhorst Pack Scheme. The spin-polarized simulation was run with a cutoff energy of 400 eV throughout the computations. Due to the periodic conditions, the vacuum layer was set to be 15 Å along z-axis to avoid interactions between neighboring images. The calculations convergence of energies was 10^{-6} eV and force was 0.01 eV/Å. In consideration of Vander Waals force between adsorptions and adsorbents, Grimme's D2 (DFT-D2) was adopted in adsorption process. As shown in Figure S21a, N_2 molecule is more likely to be captured by the Co-site in the (010) surface for CoS_2 while NS-G exhibit little absorption for nitrogen. Cobalt sulfide exhibits N_2 adsorption energy of -12.39 eV, which is lower than

NS-G (-2.09 eV). This result demonstrates that nitrogen is easier to adsorb onto the cobalt sulfide nanoparticles for CoS_2/NS-G hybrid during NRR process.

S22. The reaction kinetics and electron transport rates have been further determined using the Butler-Volmer approach.

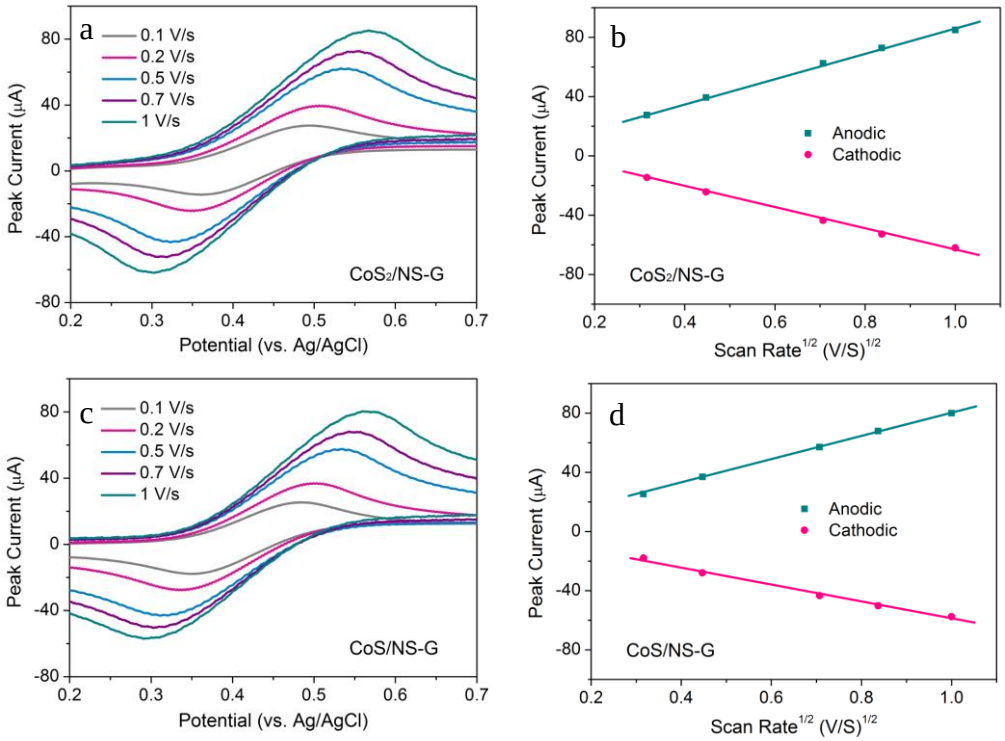

Figure S22 Variable scan rate cyclic voltammetry curves and corresponding current density vs scan rate$^{1/2}$ plot of CoS_2/NS-G (a, b) and CoS/NS-G (c, d) by using ferrocene as model analyte.

The reaction kinetics and electron transport rates have been further determined using the Butler-Volmer approach[S4,S5]. As shown in Figure S22a and S22c, the anodic and cathodic peaks separated with the increasing scan rate by using ferrocene as model analyte. The apparent rate constant of these hybrids can be calculated according to the

Laviron formalism using the following set of equation[S4]:

$$E_{p,c} = E^{o\prime} - \frac{2.3RT}{\alpha nF}\log[\frac{\alpha nFv}{RTk_{app}}]$$

$$E_{p,a} = E^{o\prime} - \frac{2.3RT}{(1-\alpha)nF}\log[\frac{(1-\alpha)nFv}{RTk_{app}}]$$

where $E_{p,a}$ is the potential of the anodic peak, $E_{p,c}$ is the potential of the cathodic peak, $E^{\circ\prime}$ is the formal potential calculated by averaging the anodic and cathodic potentials at slow scan rates, v is the scan rate, α is the electron-transfer coefficient, k_{app} is the apparent rate constant, R is the ideal gas constant, T is the absolute temperature, F is the Faraday constant, and n is the number of electrons transferred. The electron transfer rates of 19.5 s^{-1} and 7.8 s^{-1} were measured for CoS_2/NS-G and CoS/NS-G, respectively. Thus it can be concluded that CoS_2/NS-G exhibits superior charge transfer ability than that of CoS/NS-G which is consist with the XANES result.

S23. Product of hydrazine detected by the Watt and Chrisp method.

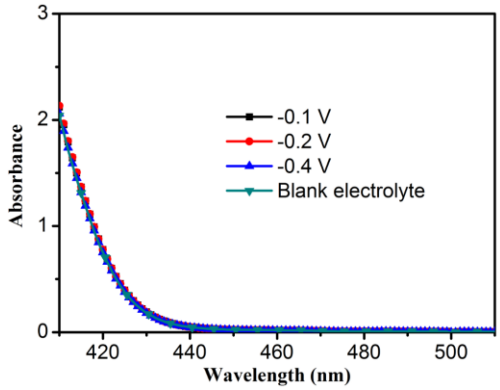

Figure S23 UV-vis absorption spectra of the electrolytes stained by the Watt and Chrisp method after potentiostatic tests under different conditions.

Chronoamperometric experiments under N_2 gas flow were implemented for CoS_2/NS-G hybrid under different potentials. The hydrazine was spectrophotometrically detected by the Watt and Chrisp method. And the absorbance at 455 nm was measured by UV-vis spectrophotometer which implies the formation of hydrazine during NRR process. The corresponding UV–Vis absorption spectra are shown in **Figure S23**, the intensity of absorption peak at 455 nm for the electrolyte tested at different potentials is the same as blank electrolyte, which suggests there was no product of hydrazine has been produced in NRR process. Therefore, cobalt sulfide hybrid cannot catalyze nitrogen being reduced to hydrazine in the electrochemical test.

S24. Charge transfer resistances of different catalysts.

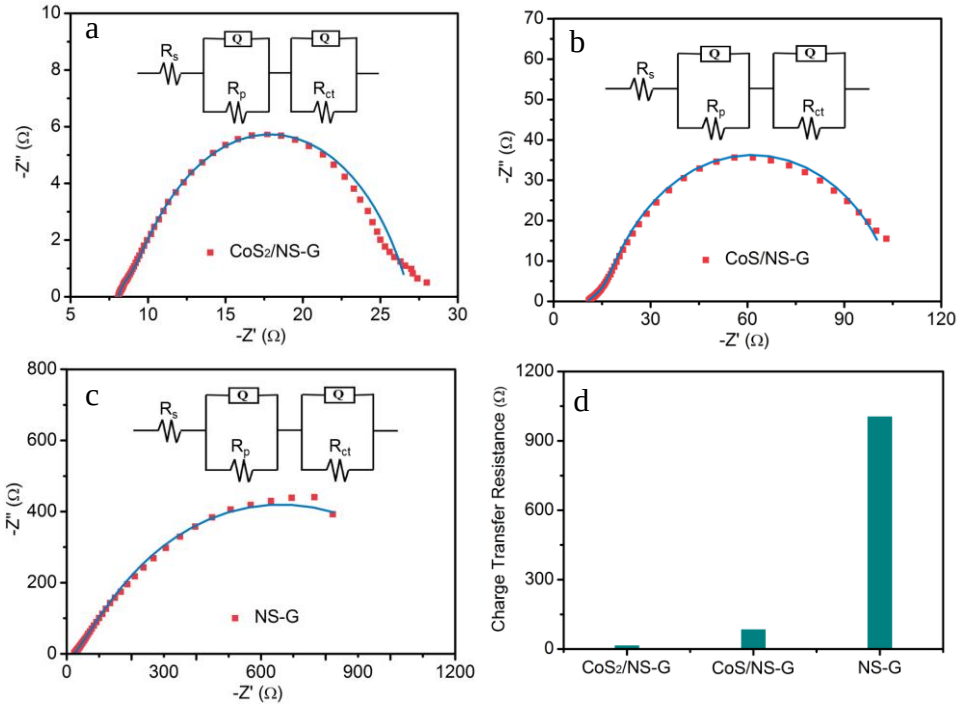

Figure S24 Nyquist plots of a) CoS_2/NS-G, b) CoS/NS-G and c) NS-G. Inset: the equivalent circuit used for fitting the Nyquist plots. d) Comparison of the charge transfer resistance (R_{ct}) of CoS_2/NS-G, CoS/NS-G and NS-G catalysts.

The as-obtained EIS data were fitted by using a simplified circuit model (Figure S24a-c insert). As shown in Figure S24a-c, two clear semicircles were observed, one in the high-frequency region related to the surface porosity and the other in the low-frequency region related to the charge transfer process. In Figure S24d, the charge transfer resistance (R_{ct}) of CoS_2/NS-G, CoS/NS-G and NS-G during NRR process are 17.9 Ω, 87.3 Ω and 1007.0 Ω, respectively. CoS_2/NS-G catalyst exhibits smallest charge transfer resistance than that of CoS/NS-G and NS-G, indicating that strong Co-N/S-C bonds lead to faster reaction kinetics by accelerating electron transfer.

S25. ^{15}N isotope labeling experiment.

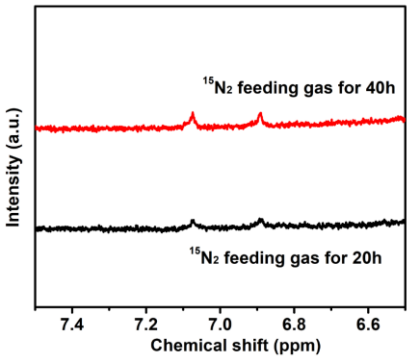

Figure S25 NMR spectra for the electrolyte after NRR test for different durations at -0.2 V in $^{15}N_2$.

S26. UV-vis absorption spectra of different electrolytes.

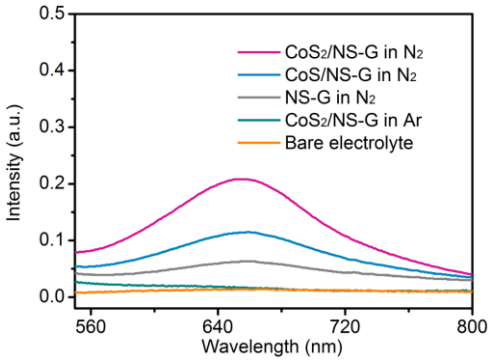

Figure S26 UV-vis absorption spectra of the electrolytes stained with indophenol indicator after potentiostatic tests under different conditions.

S27. The relationship of NH_3 yield rate and interfacial interactions.

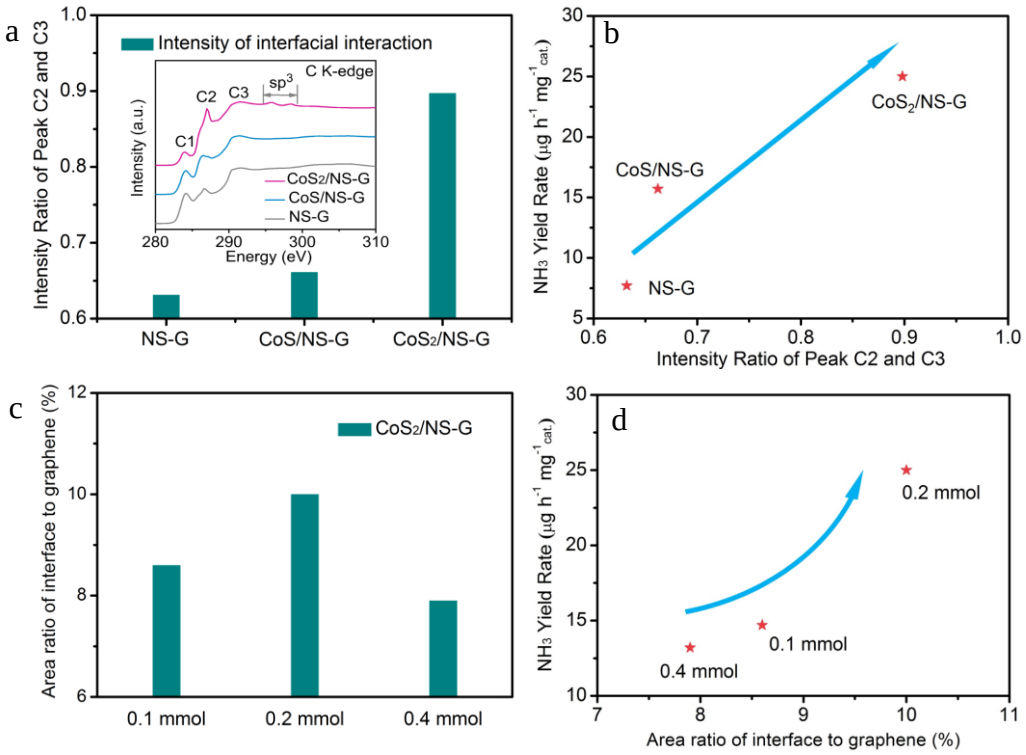

Figure S27 a) Comparison of the interfacial intensity of CoS_2/NS-G, CoS/NS-G and NS-G. Insert: C K-egde XANES spetra of CoS_2/NS-G, CoS/NS-G and NS-G. b) The relationship of interfacial intensity and NH_3 yield rate. c) Comparison of interface area of CoS_2/NS-G synthesized by different amount of cobalt salt. d) The relationship of interface area and NH_3 yield rate.

To characterize the extent of the interfacial interactions, the normalized intensity ratio of peak C2 relative to C3 are shown in Figure S27a. Compared with CoS/NS-G, CoS_2/NS-G exhibits an increased intensity ratio of C2/C3, which demonstrates that a stronger interfacial interaction was constructed in CoS_2/NS-G and would enable superior charge transfer ability for NRR. The relationship of NH_3 yield rate and interfacial interactions is summarized in Figure S27b. With the increase of interfacial interaction intensity (intensity ratio of peak C2/peak C3), the hybrids exhibits an improved NRR efficiency with NH_3 yield rate as indicator.

The interface conducting area was represented by calculating the nanoparticle area

in TEM images. Figure S27c shows the area ratio of interface to graphene support. The CoS_2/NS-G (0.2 mmol) exhibit largest interfacial area than that of 0.1 mmol and 0.4 mmol. The relationship of NRR efficiency and interface area is summarized in Figure S27d. With the increase of interface area ratio, the strong-coupled CoS_2/NS-G exhibits an improved NH_3 yield rate, which further confirms the important role of interfacial engineering.

S28. Stability test of CoS_2/NS-G for NRR.

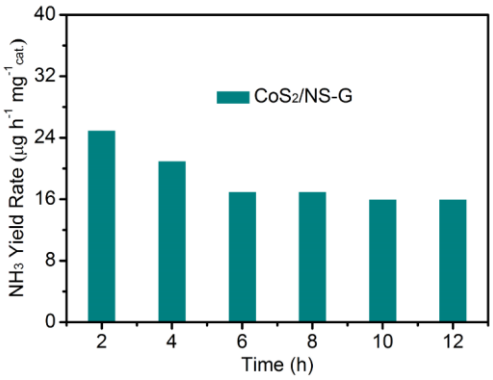

Figure S28 NH_3 yield rate at -0.2V of CoS_2/NS-G hybrid material under different reaction

Chronoamperometric experiments under N_2 gas flow were implemented to verify the NRR stability for CoS_2/NS-G hybrid. The ammonia was spectrophotometrically determined by the indophenol blue method. Figure S28 shows the NH_3 yield rate at 0.2V of CoS_2/NS-G hybrid material under different reaction time. CoS_2/NS-G exhibit good stability with NH_3 yield rate of 16.1μg h^{-1} $mg^{-1}_{cat.}$ after 12 hours constant voltage test.

Table S1. The intensity ratio of peak C1 and C2 relative to C3 in C K-edge XANES spectra of as-prepared hybrid catalysts.

Catalysts	C1/C3	C2/C3
NS-G	0.547	0.632
CoS/NS-G	0.406	0.662
CoS_2/NS-G	0.209	0.898

Table S2. Comparison of NRR catalytic performance for well-developed electrocatalysts recorded at room temperature and atmospheric pressure

	System/Catalyst	Conditions	Yield and Faradaic efficiency	Reference
Non-Noble-Metal based Electrocatalysts	Carbon rod | 0.05 M H_2SO_4| CoS_2/NS-G	Room temperature and atmospheric pressure	25.0 μg h^{-1} mg^{-1} (-0.2 V) and 25.9% Faradaic efficiency (-0.05 V)	This work
	Carbon rod | 0.05 M H_2SO_4| CoS/NS-G	Room temperature and atmospheric pressure	15.7 μg h^{-1} mg^{-1} (-0.2 V) and 15.6% Faradaic efficiency (-0.05 V)	This work
	Pt foil | 0.1 M HCl| Polymeric Carbon Nitride	20 °C and atmospheric pressure	8.09 μg h^{-1} mg^{-1} (-0.2 V) and 11.59% Faradaic efficiency (-0.05 V)	24
	Carbon rod | 0.1M KOH| MOF derived N-doped	Room temperature and atmospheric pressure	3.4×10^{-6} mol cm^{-2} h^{-1} (-0.3 V) and 10.2% Faradaic efficiency (-0.3 V)	22
	Pt plate |0.1 M HCl| $Bi_4V_2O_{11}$- CeO_2 hybrid nanofibers	Room temperature and atmospheric pressure	23.21 μg h^{-1} mg^{-1} (-0.2 V) and 10.16% Faradaic efficiency (-0.2 V)	25
	Pt plate |0.5 M Li_2SO_4| PEBCD	Room temperature and atmospheric pressure	~2.01 μg h^{-1} cm^{-2} (-0.7 V) and 2.91% Faradaic efficiency (-0.4 V)	S6
	Pt plate | 0.1 M HCl| Nitrogen-Doped Porous Carbon	Room temperature and atmospheric pressure	15.7 μg h^{-1} mg^{-1} (-0.2 V) and 1.45% Faradaic efficiency (-	23

			0.2 V)	
	Pt foil | 0.05 M H_2SO_4| N‑Doped Porous Carbon	Room temperature and atmospheric pressure	1.40 mmol g^{-1} h^{-1} (-0.9 V) and 1.42% Faradaic efficiency (-0.9 V)	S7
	Pt wire | 3.0 M KCl| Fe_2O_3-CNT	20 °C and atmospheric pressure	$2.2*10^{-3}$ g m^{-2} h^{-1}	17
Noble-Metal based Electrocatalysts	Pt mesh |0.5 M Li_2ClO_4| Au nanocages	20 °C and atmospheric pressure	3.9 µg cm^{-2} h^{-1}(-0.5 V) and 30.2% Faradaic efficiency (-0.2 V)	S8
	Carbon rod | 0.05 M H_2SO_4| Ru SAs/N-C	Room temperature and atmospheric	120.9 µg h^{-1} mg^{-1} (-0.2 V) and 29.6% Faradaic efficiency (-0.2 V)	S9
	Pt plate |0.1 M HCl| amorphous-Au/CeO_x–RGO	Room temperature and atmospheric pressure	8.3 µg h^{-1} mg_{Pd}^{-1} (-0.2 V) and 10.10% Faradaic efficiency (-0.2 V)	S10
	Pt gauze |0.1 M PBS| Pd/C	Room temperature and atmospheric pressure	4.9 µg h^{-1} mg^{-1} (-0.05 V) and 8.2% Faradaic efficiency (0.1 V)	13
	Pt plate |0.1 M HCl| Au-TiO_2 sub-nanocluster	Room temperature and atmospheric pressure	21.4 µg h^{-1} mg^{-1} (-0.2 V) and 8.11% Faradaic efficiency (-0.2 V)	11
	Pt plate |0.1 M KOH| Au nanorods	Room temperature and atmospheric pressure	1.648 µg h^{-1} cm^{-2} (-0.2 V) and ~4% Faradaic efficiency (-0.2 V)	12
	Pt plate |0.1 M KOH| PdCu/rGO	Room temperature and atmospheric pressure	2.8 µg h^{-1} cm^{-2} (-0.2V) and ~4.5% Faradaic efficiency (0 V)	14
	Carbon rod | 0.1 M KOH | Rh nanosheet	Room temperature and atmospheric pressure	23.88 mg h^{-1} mg^{-1} (-0.2 V) and ~0.65% Faradaic efficiency (0 V)	S11

References

S1. Marcano DC, et al. (2010) Improved Synthesis of Graphene Oxide. *ACS Nano* 4:4806-4814.

S2. Kresse G, Furthmüller J. (1996). Efficiency of ab-initio total energy calculations for metals and semiconductors using a plane-wave basis set. *Comput Mater Sci* 6: 15-50.

S3. Perdew JP, et al. (1996). Generalized gradient approximation made simple. *Phys Rev Lett* 77: 3865- 3868

S4. Hanna CM, et al. (2018). Interfacial Electron Transfer of Ferrocene Immobilized onto Indium Tin Oxide through Covalent and Noncovalent Interactions. *ACS Appl Mater Interfaces* 10: 13211-13217.

S5. Laviron E. (1979). The use of linear potential sweep voltammetry and of ac voltammetry for the study of the surface electrochemical reaction of strongly adsorbed systems and of redox modified electrodes. *J Electroanal Chem* 100: 263-270.

S6. Chen GF, et al. (2017) Ammonia Electrosynthesis with High Selectivity under Ambient Conditions via a Li^+ Incorporation Strategy. *J Am Chem Soc* 139:9771-9774.

S7. Liu Y, et al. (2018) Facile Ammonia Synthesis from Electrocatalytic N_2 Reduction under Ambient Conditions on N-Doped Porous Carbon. *ACS Catal* 8:1186-1191.

S8. Nazemi M, et al. (2018) Enhancing the rate of electrochemical nitrogen reduction reaction for ammonia synthesis under ambient conditions using hollow gold nanocages. *Nano Energy* 49: 316-323.

S9. Geng Z, et al. (2018) Achieving a Record ‐ High Yield Rate of 120.9 μg h^{-1} mg^{-1} for N_2 Electrochemical Reduction over Ru Single−Atom Catalysts. *Adv Mater* 30: 1803498.

S10. Li SJ, et al. (2017) Amorphizing of Au Nanoparticles by CeO_x–RGO Hybrid Support towards Highly Efficient Electrocatalyst for N_2 Reduction under Ambient Conditions. *Adv Mater* 29:1700001.

S11. Liu HM, et al. (2018) Surfactant-free atomically ultrathin rhodium nanosheet nanoassemblies for efficient nitrogen electroreduction. *J Mater Chem A* 6:3211-3217.